Granular Matter (2019) 21:61
https://doi.org/10.1007/s10035-019-0915-5

ORIGINAL PAPER

On the role of pore pressure in dynamic instabilities of saturated model granular materials

T. T. T. Nguyên[1] · T. Doanh[1] · A. Le Bot[2] · D. Dalmas[2]

Received: 21 November 2018

Abstract

Drained triaxial axisymmetric isotropic and subsequently shear compression tests are performed on fully water-saturated short cylindrical samples of nearly monodisperse glass beads, initially assembled in a loose state by moist tamping and undercompaction technique. Both *fully drained* isotropic and shear tests are affected by dynamic instabilities triggered under uncontrolled isotropic or deviatoric stress. These dynamic instabilities encompass isotropic collapses, compression stick-slips and especially the unexpected isotropic liquefaction. The most reasonable but imprecise scenario points to a possible dynamical collapse of the granular structure triggered by a spontaneous failure of the force chains, generating an instantaneous surge of excess pore pressure in a fully saturated system. This paper aims in exploring the key role of pore pressure outburst on some global macroscopic parameters of these dynamic events. It focuses on the unforeseen, short-lived and stabilised excess dynamic pore pressure and proposes an in-depth assessment of the validity and the reliability of pore pressure measurements. Irrespective of loading condition (i.e. isotropic or drained compression shear) the ephemeral stabilised excess dynamic pore pressure controls the evolution of the axial and volumetric strains in an essentially dynamic consolidation process. Some appearance conditions for these unexpected dynamic instabilities are discussed.

Keywords Dynamic Instability · Liquefaction · Stick-slip · Model granular materials · Triaxial compression · Friction

List of symbols

ε_a	Axial strain
ε_v	Volumetric strain
$\Delta\varepsilon_a$	Incremental axial strain
$\Delta\varepsilon_v$	Incremental volumetric strain
Δh	Axial displacement
Δq	Deviatoric stress drop
Δq^{norm}	Normalized deviatoric stress
Δv	Volume displacement
ΔU	Excess pore pressure
ΔU^{norm}	Normalized excess pore pressure
ΔU^{peak}	Maximum excess pore pressure in transient phase
ΔU^{stable}	Stabilised excess pore pressure in transient phase
ΔU_{bottom}	Bottom excess pore pressure
ΔU_{top}	Top excess pore pressure
ΔU_{tb}	Pore pressure difference between top and bottom
γ_w	Fluid unit weight
φ^{first}	Mobilized frictional angle at first stick-slip
φ^{max}	Mobilized frictional angle at failure
φ^{PT}	Mobilized frictional angle at phase transformation
ρ	Density
σ	Total stress
σ'	Effective stress
σ'_{ini}	Initial effective stress
σ'_{trig}	Triggering effective stress
σ_a	Axial stress
σ_r	Radial stress
e	Void ratio
e_{20}	Void ratio at 20 kPa of confining pressure
e_c	Void ratio at beginning of deviatoric shearing

Electronic supplementary material The online version of this article (https://doi.org/10.1007/s10035-019-0915-5) contains supplementary material, which is available to authorized users.

✉ T. Doanh
thiep.doanh@entpe.fr

[1] LTDS (UMR CNRS 5513), Ecole Nationale des Travaux Publics de l'Etat, 2 Rue M. Audin, 69518 Vaulx en Velin Cedex, France

[2] LTDS (UMR CNRS 5513), Ecole Centrale de Lyon, 36 Avenue Guy-de-Collongue, 69134 Ecully Cedex, France

Published online: 29 June 2019

e_{max}	Maximum void ratio
e_{min}	Minimum void ratio
e_{trig}	Void ratio at σ'_{trig}
f_U	Frequency of pore pressure at the transient phase
k	Permeability
q	Deviatoric stress
q_{trig}	Triggering deviatoric stress of slip phase
q_{stable}	Stabilised deviatoric stress
q_{vib}	Minimum deviatoric stress in transient phase
r_u	Pore pressure ratio
t_{50}	Time for 50% of consolidation
B	Skempton's coefficient
C_c	Curvature coefficient
C_u	Uniformity coefficient
C_v	Consolidation coefficient
D_0	Initial diameter
D_{50}	Average particle diameter
D_r	Relative density
D_{r20}	Relative density at 20 kPa of confining pressure
H_0	Initial height
LVDT	Linear variable differential transformer
T_v	Time factor
U	Pore pressure
U_{bottom}	Bottom pore pressure
U_{top}	Top pore pressure
U^{peak}	First peak of pore pressure
U^{stable}	Stabilised pore pressure
U_0	Back pressure
V_0	Initial volume
V_{grains}	Volume of grains
V_{void}	Volume of void

1 Introduction

Granular matter is one of the most ubiquitous materials used in civil engineering, and one of the most difficult to model, theoretically or numerically, especially for earthquake engineering. Liquefaction often occurs in loose and saturated granular layers during earthquake with devastating consequences. This phenomenon can be easily explained by the lack of granular skeleton when the granular particles are separated from each other; resulting in a null effective contact stress σ' between grains. From the effective stress principle, $\sigma' = \sigma - U$ formulated by Terzaghi [66] for totally saturated medium, σ being the total stress of the only two-phase (grains and water) element, and U the pore fluid pressure, liquefaction can be best understood as the vanishing of σ' or the equalisation of σ and U. Consequently, the measurement of the pore fluid pressure is of paramount importance to the understanding of this liquefaction phenomenon.

A large amount of experimental studies has been devoted to the measurement of U on site and in laboratory [9, 36, 55]. Cyclic or pseudo-dynamic liquefaction was first investigated in laboratories using conventional and dynamic triaxial and torsional shear machines, due to the similarity with liquefaction induced by earthquakes. Static liquefaction has next been observed in undrained or partially drained loading conditions. The pore pressure evolution was investigated in these experiments with great precision; although it was slowly and progressively generated by quasi-static loading conditions. However, the physical significance behind the pore pressure generation is far from being fully understood, excepting by the soil dilatancy mechanism, Schofield et al. [58]. One simple scalar parameter, pore pressure ratio $r_u = U/\sigma'_{ini}$ [61], was defined to identify the liquefaction level ($r_u = 1$), σ'_{ini} is the initial effective stress, often approximated in laboratory by the initial isotropic pressure in the triaxial chamber.

Centrifuge and 1-g shaking table testings complete the laboratory investigation as a useful step towards the understanding of the dynamic character of earthquakes. Recently, in-situ instrumentation has shed new light on the real time history of excess pore pressure on liquefied soils and shown the difficulty of measuring U on-site. These tests point out the dynamic aspect of U by measuring a sudden increase of pore pressure shortly after the beginning of shaking period, both in laboratory and on-site [9, 54, 69]. σ'_{ini} is taken as the initial vertical effective stress. However, many basic questions remains unanswered: What are the physical generating mechanisms and the associated controlling parameters of the pore fluid pressure?

In order to understand and explain the complexity of granular medium in laboratory testing, glass beads are frequently used as a simplified analogue material in soil mechanics [1], in physics [29] and geophysics [59].They served as a natural complement to the use of spherical grains in numerical discrete element modelling (DEM). These model materials lead to the discovery of the stick-slip phenomenon in triaxial compression and simple shear [2, 10, 18, 47, 74, 76]; and recently to the totally unexpected collapse and liquefaction during isotropic drained compression or consolidation [15, 16]. These events, termed as dynamic instabilities, are probably different facets of the same physical phenomenon and are strongly related to the spontaneous generation of the pore fluid pressure. Excepting the rare case of de-structuration on calcarenite in isotropic compression, with unknown dynamic features [38], and the case of liquefaction of Eniwetok sand happening during the first unloading under isotropic undrained cycle of high pressures [22], these dynamic instabilities were unknown to granular science prior to our works, especially the coupled volumetric stick-slip, the fast transition from solid-like to liquid-like behaviour and the isotropic liquefaction. To our knowledge, they have never been predicted theoretically, despite a large number of advanced constitutive models for geomaterials [12, 27, 34, 40, 45, 49, 72], nor detected in

Table 1 Index properties of SLG 6-8 glass beads

Property	Value
Density, ρ (kg/m^3)	2500
Mean size, D_{50} (mm)	0.723
Uniformity coefficient, C_u	1.463
Curvature coefficient, C_c	0.989
Maximum void ratio, e_{max}	0.686
Minimum void ratio, e_{min}	0.574

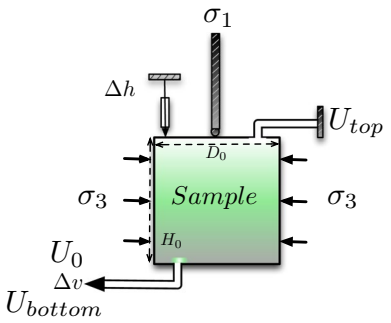

Fig. 1 Schematic view of the experimental setup for isotropic consolidation and drained triaxial compression

numerous numerical DEM experiments with spherical particles [43, 44, 57, 62, 63], including a full solid–liquid coupling formulation [19, 25, 26], and instabilities [23].

Our previous studies also rule out the possibility of the dynamic pore fluid pressure being the primary cause of these events, and extend a step further the conjecture of dynamic pore pressure fluctuations formulated earlier in rapid shearing experiments [31].

Given the important place of pore fluid pressure in completely saturated materials, the objectives of this paper consist of a study of the unexpected effects of short-lived stabilised excess pore pressure on the axial and volumetric strains of these dynamic instabilities. It also includes an in-depth verification of the pore pressure measurements and stresses the importance of their accuracy, especially for dynamic events.

Section 2 describes the experimental setup designed for testing idealized granular materials and the sets of laboratory tests. The usual global behaviour under drained isotropic and vertically sheared compression is strongly affected by unexpected "stick-slip" like events. These remarkable dynamic instabilities are rapidly reported in Sect. 3, together with the assessment of the validity of the excess pore pressure measurements. The effects of the ephemeral stabilised pore pressure of these spontaneous dynamic events in compression loading, including the rare events in isotropic liquefaction and undrained compression stick-slip, are examined in Sect. 4. Finally, the paper discusses some conditions for the appearance of these unexpected dynamic instabilities and highlights some essential concluding remarks in the last section.

2 Experimental programme

Virgin monodisperse and spherical soda-lime glass beads (CVP Sil-glass) of mean diameter of 0.723 mm, commercialized by CVP, Linselles, France,[1] are used in each experimental test to avoid possible wearing effects. These beads can be classified as clean and poorly graded fine-grained granular materials with usual index properties reported in Table 1.

The classical experimental system is used in this study for triaxial testing on a short cylindrical specimen of initial height $H_0 = 70$ mm and diameter $D_0 = 70$ mm inside a triaxial cell [36]. The sample is a granular assembly enclosed inside a cylindrical and open-ended latex membrane of 0.3 mm thickness which is closed by a duralumin top cap when introduced in the loading cell. Loose and very loose model granular samples are created using modified moist tamping and under compaction method [8, 35]. Predetermined quantities of moist glass beads, mixed with 2% of distilled water by weight, are placed and gently compacted in five layers of prescribed thickness using a flat-bottom tamping circular stainless steel rod of 20 mm in diameter. A fully saturated state is obtained using CO_2 method [37] with de-aired distilled water, together with a high back pressure of 200 kPa. High Skempton's coefficient $B = \Delta U/\Delta\sigma \geqslant 0.95$ [64] assesses the fully saturated system. Additional information can be found in our previous works on sands [17, 28].

The initial structural anisotropy of model granular assembly created by moist-tamping method is one of the required conditions for the appearance of these instabilities [16].

In this study, Fig. 1 presents a special experimental set-up to fully quantify the pore pressure evolution for the unexpected instabilities during the isotropic consolidation and compression shearing.

Constant back pressure U_0 needed for a full saturation is applied at the bottom of the sample. Since U_0 is imposed from the bottom drainage, the top pore-water pressure U_{top} is recorded close to the duralumin top cap of the granular sample to ensure a homogeneous stress state. Additionally, the bottom pore-water pressure U_{bottom} is measured to check the evolution of back pressure during dynamic instabilities. The data is synchronously acquired at 10 kHz with a dynamic data acquisition system NI 4472B of National Instruments. The static top pore-water pressure U_{top} is recorded by a piezoresistive transducer (Sedeme, MD20)

[1] www.Cvp-abrasif-broyage.com.

with unknown resonant frequency. It is located outside the triaxial cell using a very thick plastic tube (Swagelok PFA) connected to the top cap of the granular sample, in a dead-end at a distance of about 60 cm. A dynamic piezoelectric pore pressure sensor (PCB S112A21) is also used in this experimental setup at 10 cm preceding the static one, having high resonant frequency (250 kHz). The bottom pore-water pressure U_{bottom} is measured by another transducer (Kistler, 4053A10) with natural frequency of about 120 kHz. It is also situated outside the triaxial cell at a distance of about 10 cm from the bottom platen and completed by another dynamic pore pressure sensor (PCB S112A21) in the same position.

Although miniature mid-plane pore pressure sensors can be an option in the triaxial experiment to assess these pore fluid responses [65]; unfortunately, their use is still problematic with very loose granular sample.

A classical triaxial test consists of two successive loading steps: isotropic consolidation or isotropic drained compression followed by drained vertical shearing in compression only if the sample is still geometrically stable. Compressed air under constant stress rate (1 kPa/s in our case) is used in the first isotropic step to bring the sample up to a desired cell pressure $\sigma'_r = \sigma'_3$, the minor principal stress. In the second step, the sample is subsequently sheared vertically under constant σ'_r and constant axial strain rate (0.0048%/s) in drained or undrained condition. This second step adds an additional deviatoric shear stress $q = \sigma'_a - \sigma'_r$ to the first purely isotropic step; $\sigma'_a = \sigma'_1$ is the axial (major principal) stress. The excess pore pressure $\Delta U = U - U_0$ is kept low—to a few kPa—to respect the requirement of full drainage for these two successive steps. The global axial strain $\varepsilon_a = \Delta h/H_0$ is estimated with the measurement of axial displacement Δh, using LVDT sensor, of the top platen inside the triaxial cell. The global volumetric strain is deduced from $\varepsilon_v = \Delta v/V_0$, where V_0 is the initial sample volume, and Δv the water volume expelled from or moved into the sample. The volumetric strain is usually translated into void ratio e in the first isotropic step. Following the usual convention in soil mechanics, volumetric and axial strains are positive (respt. negative) for compaction (respt. dilation).

Since the vertical loading ram is not physically connected to the top cap, the cylindrical sample is not kinematically constrained and it is free to deform, vertically and horizontally.

3 Experimental results

Since the temporal evolution of pore fluid pressure during the dynamic collapse and slip phase in triaxial testing is of particular interest, this paper is focused on the pore pressure measurements U_{top} and U_{bottom}, as well as the pore pressure difference $\Delta U_{tb} = U_{top} - U_{bottom}$.

Figure 2 gives some essential notations of the temporal evolution of deviatoric stress q and pore pressure U during laboratory dynamic instabilities. The pore pressure changes from constant back-pressure U_0 to the first short-lived peak U^{peak}, then reduces to the stabilised U^{stable} before returning down to U_0. The deviatoric stress drops from q_{trig} towards the first minimum q_{vib} before returning to the steady-state q_{stable}. ΔU^{stable} is the brief stabilised excess pore pressure and Δq the deviatoric stress drop of the dynamic instability event.

In Fig. 3, we observed dynamic instabilities that occur in an isotropic consolidation from 20 up to 500 kPa and subsequently on a drained shear compression test at 500 kPa of confining pressure on very loose model granular materials. Four isotropic collapses, noted A to D, and 13 drained compression stick-slips, noted SS1 to SS13, are reported for this particular test.

Table 2 summarises different values measured to characterise the dynamic instabilities of this study. σ'_{trig}(respt. q_{trig}) is the uncontrolled triggering isotropic (respt. deviatoric) stress of the isotropic (shear) test. U_{top} (U_{bottom}) the interstitial pore water pressure at sample top (bottom) with the first peak U^{peak}, the stabilised value U^{stable} and the vibration frequency f_U; $\Delta\varepsilon_v$ ($\Delta\varepsilon_a$) the incremental volumetric (axial) strain produced during the instability event; Δq the deviatoric stress drop of the dynamical slip component of the stick-slip event and t_{50} the time for 50% of excess pore pressure dissipation. This very loose model granular sample has an initial void ratio (relative density $Dr = (e_{max} - e)/(e_{max} - e_{min})$) at the beginning of the isotropic consolidation at 20 kPa, $e_{20} = 0.707$ ($Dr_{20} = -19\%$).

3.1 Global behaviour

The isotropic compressibility from 20 to 500 kPa of Fig. 3a shows a very different compressibility behaviour of model granular materials from the traditional one of sands or powders [3, 66]. Instead of the expected smooth and continuous decrease of void ratio $e = V_{void}/V_{grains}$ with increasing effective stress, four isotropic collapses at uncontrolled triggering stress σ'_{trig} of 108, 188, 447 and 451 kPa can be seen with a large unexpected drop Δe. Between two collapse events, classical continuous decrease of e is observed. Two large, nearly cascading events C and D, occur just before reaching the required 500 kPa of confining pressure of the drained triaxial compression. Double or cascading collapse is observed for the second and third collapses; however, no isotropic liquefaction is noticed. Dynamic isotropic collapse is defined as spontaneous increase of axial and volumetric strains due to sudden pore pressure development at constant cell pressure, while preserving the initial cylindrical sample shape.

Table 2 Isotropic collapses from 20 to 500 kPa and drained compression stick-slips at 500 kPa of confining pressure on very loose model granular materials, $e_{20} = 0.707 (Dr_{20} = -19\%)$, with 200 kPa of back pressure

Event	σ'_{trig}/q_{trig} (kPa)	U_{top}			U_{bottom}			$\Delta\varepsilon_v$	$\Delta\varepsilon_a$	Δq
		Peak (kPa)	Stable (kPa)	Frequency (Hz)	Peak (kPa)	Stable (kPa)	Frequency (Hz)	Volume (%)	Axial (%)	Deviatoric stress drop (kPa)
Isotropic collapses from 20 to 500 kPa										
A	108	278	245	37	202	202	33,119	0.12	0.17	–
B (double)	188	473	311	46	240	240	145	0.65	0.03	–
C (double)	447	1032	500	61	437	437	145	0.82	0.14	–
D	451	971	466	59	420	399	149	0.67	0.002	–
Drained compression stick-slips at 500 kPa										
SS1	475	424	280	45	244	219	146	0.13	0.29	353
SS2	545	526	309	48	244	219	138	0.21	0.38	403
SS3	655	525	309	49	287	227	138	0.21	0.39	522
SS4	714	401	274	45	244	219	149	0.13	0.28	478
SS5	715	651	356	53	244	219	138	0.25	0.53	601
SS6	782	403	244	41	244	219	32,152	0.23	0.16	454
SS7	783	572	356	50	244	219	138	0.24	0.50	624
SS8	774	807	407	57	244	219	137	0.31	0.77	709
SS9	799	755	392	56	307	247	136	0.33	0.73	708
SS10	805	378	273	45	244	219	32,151	0.23	0.31	557
SS11	798	318	250	44	244	219	32,150	0.27	0.27	508
SS12	788	726	392	56	244	219	137	0.33	0.72	704
SS13	900	583	358	54	244	219	136	0.30	0.57	688

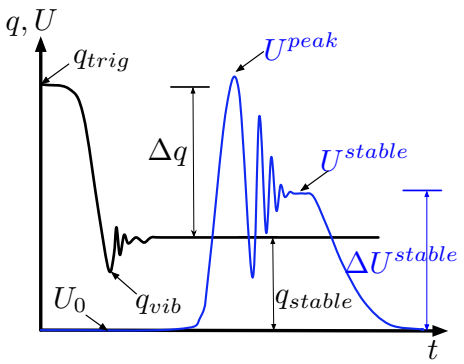

Fig. 2 Schematic view of the temporal evolution of deviatoric stress q and pore pressure U during laboratory dynamic instabilities

At the end of the isotropic consolidation at 500 kPa, Figs. 3b and c give the results of the subsequent drained compression shear. Again, instead of the expected smooth stress-strain relationship with continuous increase of q, without peak, with increasing ε_a for an initially loose granular assembly, stick-slip phenomenon is observed with quasi-periodic and large stick-slip events in Fig. 3b. Each event invariably has two phases. A first fast slip phase presents a very abrupt deviatoric stress drop Δq at also uncontrolled triggering stress q_{trig}; followed by a slow stick phase with a gradual hardening up to at least the previous deviatoric stress level, before the occurrence of the next stick-slip cycle. Quasi-regular stick-slips happen throughout the performed axial strain range, up to 25%. The largest drop towards the isotropic stress state around 25% of ε_a is a simple unloading-reloading cycle with no stick-slip in unloading. Some precursors with small Δq can be seen, as before SS4 and SS9 (open circles). On the nearly horizontal critical state plateau at q^{max}, the stick phase systematically presents a stress peak of an apparent dense behaviour, while a nearly smooth envelop curve is retrieved, conforming to the usual behaviour of loose granular materials.

The strongly coupled behaviour is noticed with the presence of large and quasi-periodic stick-slips in the evolution of volumetric strains in Fig. 3c and a constant critical state at 2.5% of ε_v, confirming the loose character previously noted on the stress-strain relationship. The sawtooth volumetric profile seems to oscillate around this critical value. The loose model granular system constantly changes, and never reaches a steady state, in terms of stress and strain. Drained compression stick-slips always have a sudden volumetric compaction in the slip phase, and a gradual dilation in the stick phase.

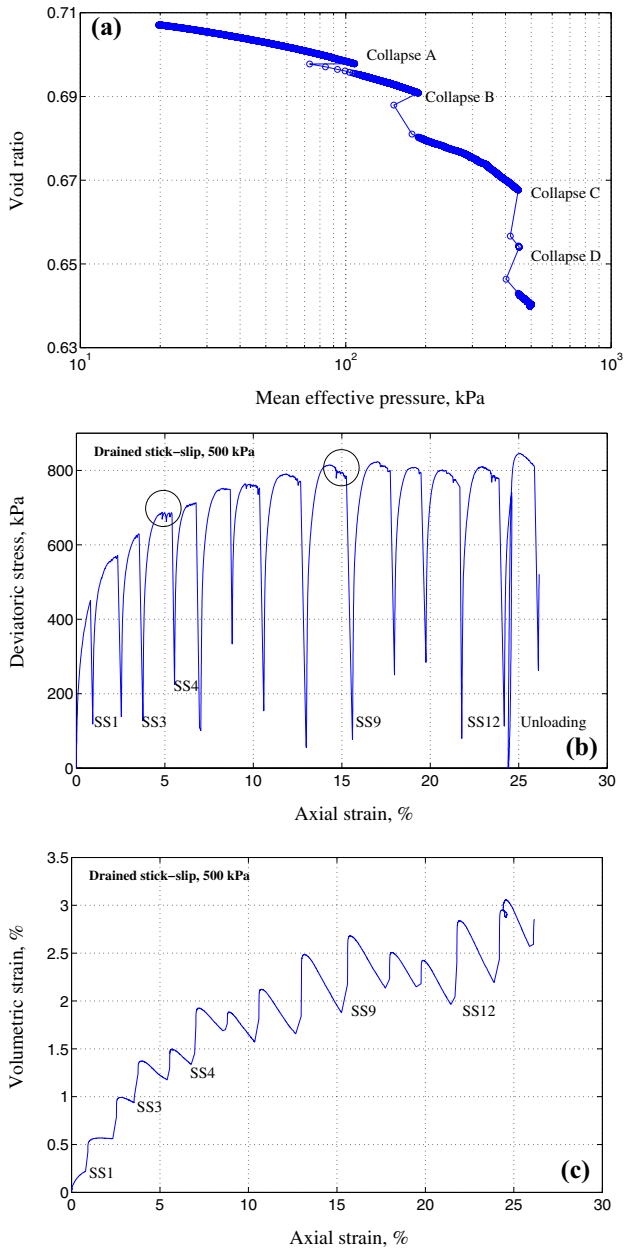

Fig. 3 **a** Isotropic instabilities from 20 to 500 kPa and **b** drained compression stick-slips with **c** coupled volumetric behaviour at 500 kPa of confining pressure on SLG 6-8 glass beads of 0.7 mm of diameter

Figure 3 adds the isotropic collapses during the unavoidable isotropic consolidation phase prior to the drained compression shearing with stick-slips. The mobilized frictional angle at failure ($\varphi^{max} = 26°9$), at first stick-slip ($\varphi^{first} = 18°4$) and at the phase transformation ($\varphi_{PT} = 18°2$) strengthen previous findings [18].

The isotropic collapse and the drained compression stick-slip seem to share some common triggering mechanisms.

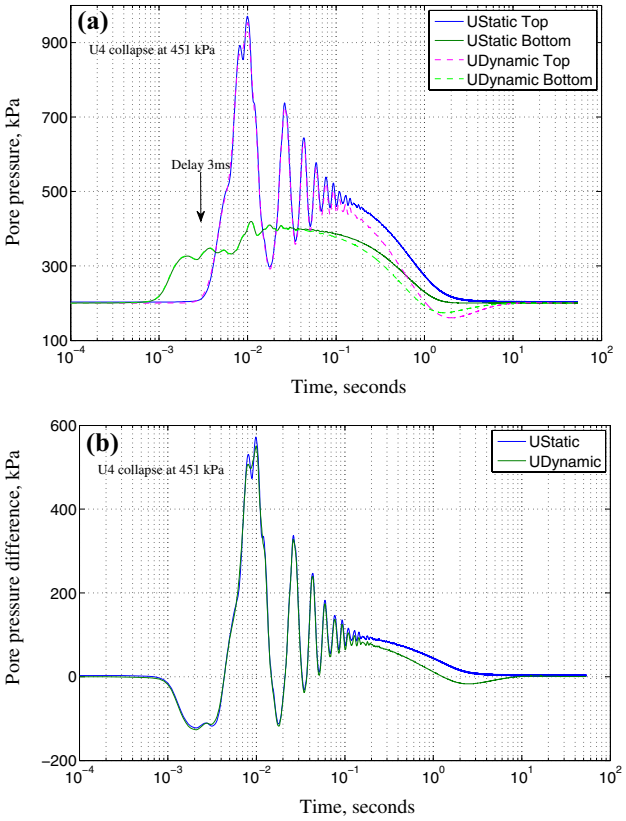

Fig. 4 **a** Temporal evolution of dynamic and static pore pressures at sample top and bottom, **b** dynamic and static pore pressure difference between top and bottom of isotropic collapse D at 451 kPa of confining pressure on 0.7 mm CVP beads

3.2 Isotropic collapses

Figure 4a presents the temporal evolution of the pore pressure U concerning the fourth isotropic collapse D at 451 kPa, rapidly occurred after collapse C as a typical result for an isotropic collapse. The time origin is shifted to the beginning of the transient phase ± 0.1 ms, which is the current time resolution. A semi-logarithmic scale is used to emphasise the suddenness of the time-related variations of U. The static pore pressure at the sample top U_{top} (solid blue line) commences with a sudden surge up to 971 kPa, U_{top}^{peak}, from constant back-pressure U_0, followed by a rapid dissipation from a short-lived stable value of 466 kPa, U_{top}^{stable}, within a few seconds towards the equilibrium state of U_0. The static pore pressure U_{bottom} (solid green line) rises earlier, up to only 420 kPa at nearly 3 ms before U_{top}. A stabilised excess bottom pore pressure $\Delta U_{bottom} = U_{bottom} - U_0$ of 199 kPa is briefly obtained despite a completely open drainage system at the bottom platen and a slow increase of cell pressure to respect the isotropic consolidation condition with constant back-pressure U_0. U_{bottom} also mildly oscillates at higher frequency than U_{top}. The small variation of U_{bottom} is probably

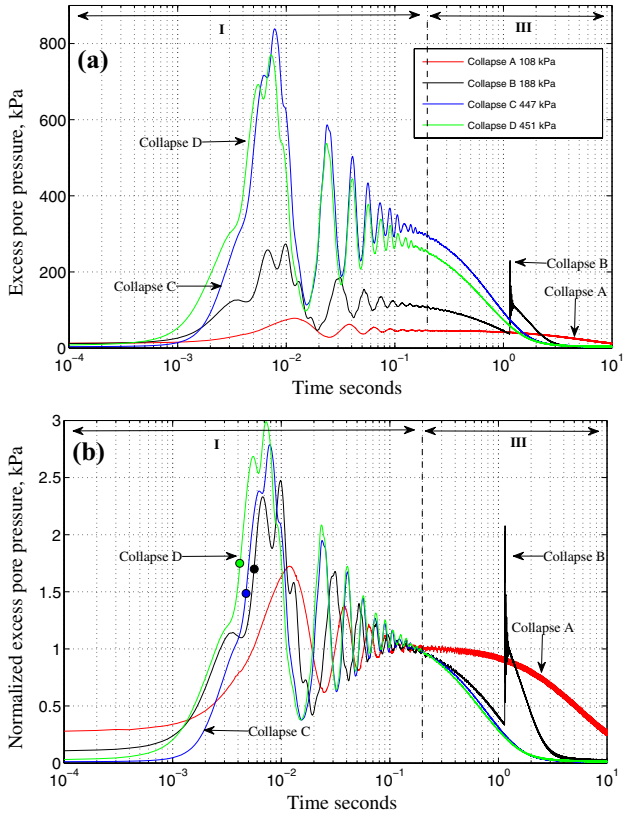

Fig. 5 **a** Temporal evolution of natural and **b** normalised static top excess pore pressures of isotropic collapses from 20 to 500 kPa of confining pressure on 0.7 mm CVP beads

linked to the open end of the drainage system and the large oscillated phase of U_{top} to the top cap drainage end.

The complementary dynamic measurements of top and bottom pore pressures (dashed lines) exactly follow the static ones in the transient phase. Unfortunately, no explanation can be found for the discrepancies at the end of the dissipation phase, when the dynamic pore pressures go unexpectedly and briefly below the imposed constant back pressure U_0 of 200 kPa before returning to the steady state U_0.

The static and dynamic pore pressure difference is shown in Fig. 4b, confirming the briefly non-homogenous effective stress state within ± 100 kPa and the presence of the unexpected transient phase. These ephemeral signals from pore pressure measurement are ripples in time, probably created by powerful events such as the destruction of chain forces. They can even lead to cataclysmic liquefaction-like phenomenon [16]. Furthermore, the result shown in Fig. 4 is essentially a monochromatic audible signal, basically with only one frequency being emitted, Table 2.

3.3 Excess pore pressure development

Figure 5a shows the spontaneous development of U_{top} for all four isotropic collapses, as the largest pore pressure inside the granular sample, due to the closed-ended (open-ended) of the top (bottom) drainage system. The second collapse is a rare event which presents a secondary collapse occurring during the dissipation phase. Large σ'_{trig} creates large U_{top}^{peak} and U_{top}^{stable}; however, U_{top}^{stable} occurs at constant time of 0.2 s.

After normalising the excess pore pressure by ΔU_{top}^{stable}, a more coherent picture of ΔU^{norm} is revealed in Fig. 5b with some discrepancies of U_{top}^{peak}. As usual for isotropic collapse case, the evolution of U_{top} and ΔU^{norm} can be reasonably broken-down into two phases. First a fast transient phase *I* occurred within 200 ms (vertical dashed line in Fig. 5). It is characterise by a damped oscillated behaviour of pore pressure which briefly stabilised after 200 ms at unity level of ΔU^{norm}. The next long dissipation phase, termed phase *III*, is of about 5 s where the pore pressure gets back to its initial equilibrium value U_0. Contrary to isotropic liquefaction which will be discussed later in the paper, we do not observed any intermediate phase, termed phase *II*, of the pore pressure maintained at constant ΔU_{top}^{stable} in between those two phases.

The existence of constant pore pressure during intermediate phase *II* for at least 1 s above 95% of ΔU_{top}^{stable} is one of three mandatory experimental conditions for isotropic and drained compression liquefaction [16]. The absence of this crucial phase leads to isotropic collapse and drained compression stick-slips.

Superimposed liquefaction points (solid circles) on the rising edge indicate the ΔU^{norm} levels close to unity ($r_u = 1$ or $\sigma = U$) in Fig. 5b. These levels correspond to a briefly null effective stress state for less than 5 ms or a short-lived local liquefaction with very limited deformation. They show a large contrast with the normal full global liquefaction always associated with runaway deformation and a total destruction of the granular skeleton [16]. The absence of a liquefaction point on the first collapse simply means a non-liquefaction event for the whole collapse. The very short duration of the stabilised phase *II* in the performed test is not long enough to bring local liquefaction to a global level of the whole granular sample.

3.4 Drained stick-slips

The large 9th stick-slip is chosen as a typical case of stick-slip behaviour in Fig. 6. The simultaneous static and dynamic measurement of top and bottom pore pressures give the impression of déjà vu despite the presence of deviatoric stress in this shearing phase. The decomposition of U in two transient and dissipated phases is very similar to isotropic

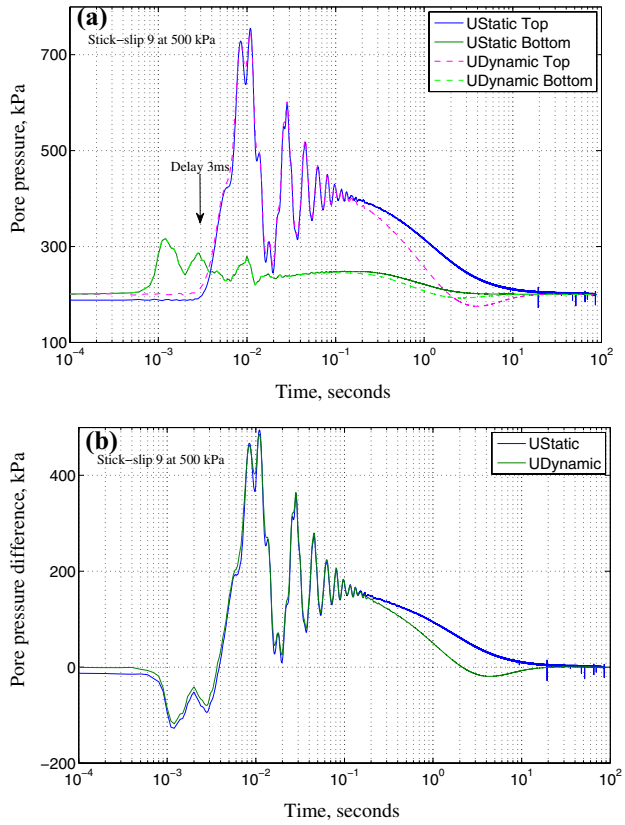

Fig. 6 **a** Temporal evolution of top and bottom dynamic and static pore pressures, **b** pore pressure difference between top and bottom of stick-slip SS9 at 500 kPa of confining pressure on 0.7 mm CVP beads

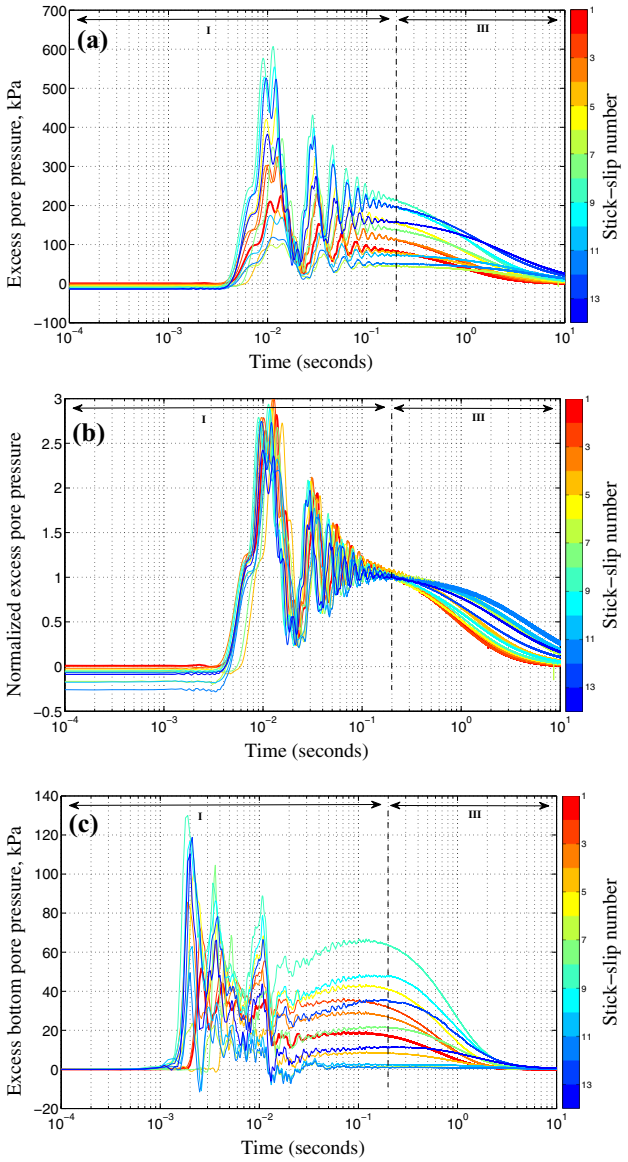

Fig. 7 Temporal evolution of **a** natural, **b** normalised static top and **c** natural bottom excess pore pressures of drained compression stick-slips at 500 kPa of confining pressure on 0.7 mm CVP beads. The stick-slip number is on the right colorbar

collapse. A fast rise to U_{top}^{peak} within 10 ms, a brief presence of U_{top}^{stable} at 0.2 s before being dissipated, a small delay of 3 ms of U_{bottom} before U_{top} in Fig. 6a, a local liquefaction event with a short-lived pore pressure above 500 kPa, a resulting non-homogenous effective stress state in Fig. 6b and the validity of unanticipated U by two different measurement techniques.

Figure 7a shows the temporal evolution of static excess top pore pressure for all stick-slips identified by their number on the right colorbar with increasing axial strain at the beginning of stick-slip event. This figure offers no pertinent analysis excepting the creation of large U_{top}^{peak} and U_{top}^{stable} as function of triggering deviatoric stress q_{trig}. The normalised ΔU^{norm} in Fig. 7b gives a more coherent picture with a single frequency during the transient phase and a possible classification of the dissipation phase as function of q_{trig}. However, no suitable analysis, such as normalised U_{bottom}^{norm}, can be found for U_{bottom} in Fig. 7c. Note the continuous increase of U_{bottom} towards the stabilised value long after the transient phase *I*.

So the pore pressure measurements always come up in pairs, counter-intuitive but measurable from sample top and bottom. Due to the bottom drainage condition, U_{bottom} is always smaller than U_{top}. Additionally U_{bottom} always happens earlier than U_{top} for about 3 ms. A pair of fluid pore pressures come up fast through the two opposite sides of the drainage system, then down again. According to the granular physics that we know for a consolidation condition, they should not be there; but they were, irrespective of the loading condition, isotropic or triaxial compression shear, and of fabrication procedure, moist tamping or even dry deposition. Note that no excess top and bottom pore pressures are detected during the unloading-reloading cycle.

This counter-intuitive surge of pore pressure is of paramount importance in understanding these newly observed dynamic instabilities. The simultaneous measurements of

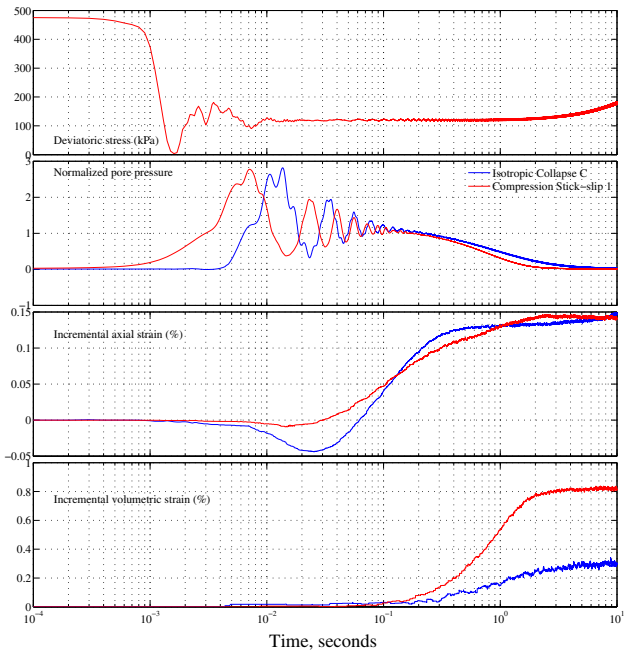

Fig. 8 Typical temporal evolution of isotropic collapse C (blue) and drained compression stick-slip SS1 (red) on 0.7 mm CVP beads : deviatoric stress, normalised excess pore pressure, axial and volumetric strain (color figure online)

pore pressure at sample top and bottom by two complementary techniques rule out the possibility of their false detection, of their creation by artefacts and reduce the margin of experimental error.

The observed pore pressure evolution during and beyond the slip phase is qualitatively similar to that measured in double-direct shear experiment with saturated granular gouge [59], or under extreme conditions during earthquakes [7], impacts [33], or blast waves [30], without the regular oscillation of the transient phase *I*. However, the instabilities in our experiments, especially liquefaction (section 4.2), surprisingly occur at moderate overpressure ($\leqslant 1$ MPa), low stress rate ($\leqslant 1$ kPa/s), ambient temperature and without any known external blast-induced loadings.

For completeness, the complementary time evolution of ε_v, ε_a, ΔU^{norm} and the additional deviatoric stress for the first drained stick-slip (red) is given in Fig. 8 on the same logarithmic scale for the time axis. These temporal evolutions are quite similar to those of spontaneous collapse under isotropic consolidation (blue) with the exception of a suddenly large deviatoric stress drop Δq to a constant level in less than 2 ms, prior to the development of ΔU with 3 ms delay, with respect to Δq. Regardless of Δq, this constant slip duration is much shorter than that obtained from sheared granular layers of glass beads [2, 48, 59], indicating a more fragile behaviour. These figures reveal fast, although continuous, overall axial contraction and volumetric compaction from a steady-state to another, within only 2s, contrasting the axial and volumetric jumps of the literature [1, 2, 10, 18, 59, 76]. Currently, no suitable explanation can be found for the unexpected small axial extension, although noticeable, during the transient phase. These observations strongly suggest a dynamic character of slip phase, and a dynamic regime for all observed granular instabilities. A complete time-resolved analysis of stick-slip phenomenon in triaxial compression of model granular media will be published elsewhere.

4 Analysis and discussions

After the assessment of the validity and the reliability of the excess pore pressure measurements, we will now focus on the effects of dynamic stabilised excess pore pressure on some global macroscopic parameters (incremental volumetric strain $\Delta\varepsilon_v$, incremental axial strain $\Delta\varepsilon_a$ and deviatoric stress drop Δq in the case of compression shear stick-slip). We also explore the rare case of isotropic liquefaction and measure the pore pressure responses under varying drainage condition as in undrained compression stick-slip.

4.1 Effects of dynamic stabilised excess pore pressure ΔU^{stable}

After checking the validity of pore pressure measurements, one logical question arises instantly: what are the effects of ΔU^{stable} on the other measuring macroscopic parameters?

Typical pore pressure and strain measurements in Fig. 8 for isotropic collapse and compression stick-slip paint a curious picture of a new type of dynamic instability of granular material, as the granular assembly has completely free drainage making collapses an unlikely condition.

For isotropic consolidation, the dynamic collapse triggered by uncontrolled σ'_{trig} creates a sudden increase of pore pressure up to a likely maximum ΔU^{stable}_{top} or a decrease of σ'. Consequently, a dissipation phase follows in order to return to the previous level of σ'_{trig}. Similar reasoning applies for drained stick-slip with constant radial stress. As indicated in Fig. 8b, dynamic instability is essentially a consolidation process under constant deviatoric stress q.

Figure 9a first explores the relationship between ΔU^{stable}_{top} and the incremental volumetric strain $\Delta\varepsilon_v$ during the isotropic collapse and during the slip component, in a usual semi-logarithmic scale in soil mechanics.

A power law relationship is obtained with high correlation, irrespective of different loading schemes: isotropic or compression shear. It means $\Delta\varepsilon_v$ is essentially controlled by the dynamic ΔU^{stable}_{top}. In the present case of constant radial stress at 500 kPa, this power law predicts 1.5% of $\Delta\varepsilon_v$ for the liquefaction case when $U^{stable} \approx 500$ kPa, or $\sigma' \approx 0$ kPa. This

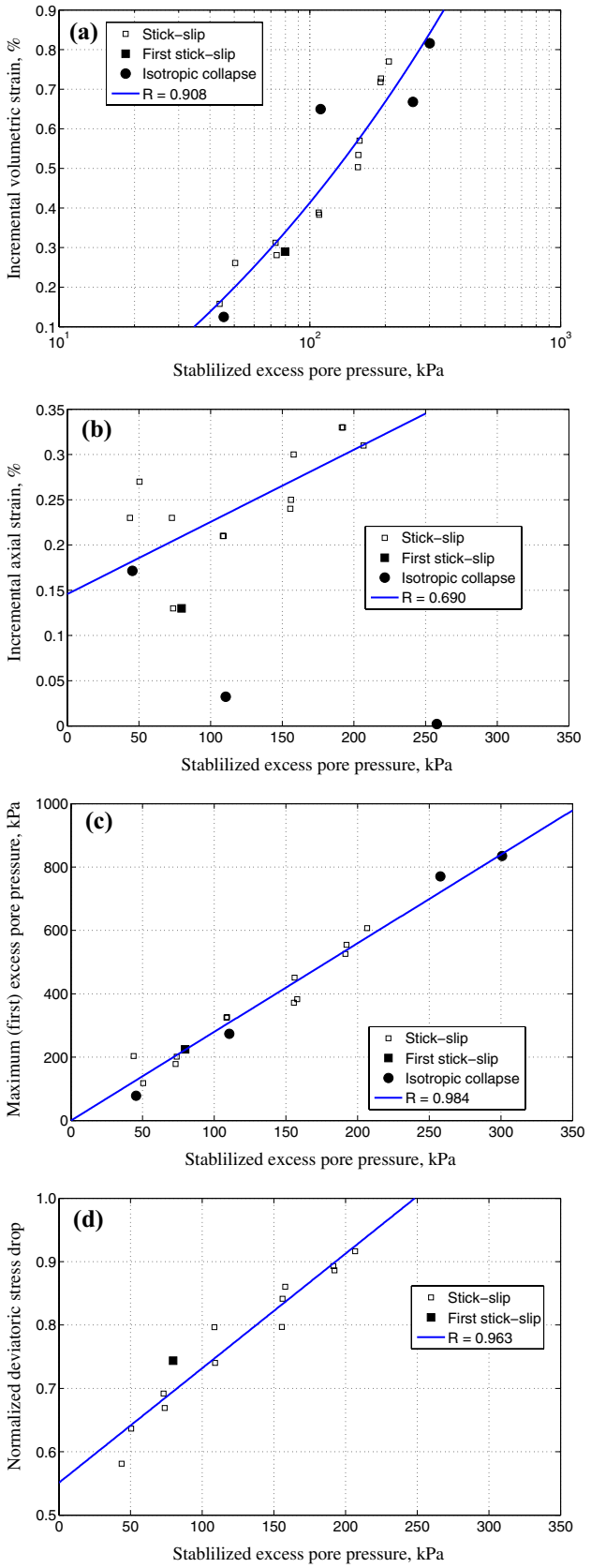

Fig. 9 Effects of dynamic stabilized excess pore pressure on **a** incremental volumetric strain $\Delta\varepsilon_v$, **b** incremental axial strain $\Delta\varepsilon_a$, **c** dynamic excess pore pressure peak ΔU_{top}^{peak} and **d** normalised deviatoric stress Δq^{norm}

predicted value slightly underestimates the real isotropic liquefaction case [16].

Since an initial structural anisotropic state is one of the two basic required components in creating these dynamic instabilities, the effects of ΔU_{top}^{stable} on the complementary incremental axial strain $\Delta\varepsilon_a$ are examined in Fig. 9b. A linear relationship is only found for stick-slip event (i.e. without isotropic collapses) with medium correlation coefficient R, meaning ΔU_{top}^{stable} is still a meaningful parameter in controlling $\Delta\varepsilon_a$ in stick-slip experiment.

Concerning the mysterious transient phase I, ΔU_{top}^{peak} is strongly related to ΔU_{top}^{stable} in Fig. 9c with excellent correlation coefficient. It seems that the observed dynamic time evolution of ΔU during the oscillating transient phase I can be modelled by the classic second-order equation of vibrating system with only two parameters (damping factor ζ and natural frequency ω_n) [71].

These three phenomenological correlations point to the key role of dynamic pore pressure ΔU_{top}^{stable} in generating $\Delta\varepsilon_v$ and $\Delta\varepsilon_a$, even if ΔU is not the real primary cause [16]. It is even disturbing to note the control of the very short-lived ΔU_{top}^{peak} on ΔU_{top}^{stable}, $\Delta\varepsilon_v$ and $\Delta\varepsilon_a$, or in-summary, on the mechanical behaviour of the dynamic consolidation under constant q.

For stick-slip case, Fig. 9d investigates the links between ΔU_{top}^{stable} and the normalised deviatoric stress $\Delta q^{norm} = \Delta q/q_{trig}$. This normalisation eliminates the dependency on q_{trig} and enables the comparison of different stick-slip experiments. $\Delta q^{norm} = 1$ denotes largest stick-slip, transforming the solid-like state to liquid-like one with no shear stress ($q \approx 0$), and generating the largest ΔU_{top}^{stable}. Liquefaction state follows if this largest ΔU_{top}^{stable} can be maintained for some seconds.

Note that the synchronised measurements of U_{top} and U_{bottom} means an instantaneous reduction of effective stress σ', according to the effective stress principle, followed by a gradual recovery. These pore pressure measurements are visible indicators that the effective stress is out of balance. It means a very brief non-homogenous effective stress state inside the sample during the short-lived collapse for less than 4 s. U_{top} vibrates like an oscillating underdamped system with a dominant frequency using power spectral density. The systematic double check of U_{top} and U_{bottom} by dynamic and static sensors eliminates the instrumental artefacts of the measured pore fluid pressure.

4.2 Isotropic liquefaction

Another question ensues: what are the static and dynamic pore pressure measurements in the special case of isotropic liquefaction with the presence of an additional phase *II* of constant ΔU^{stable} [16]?

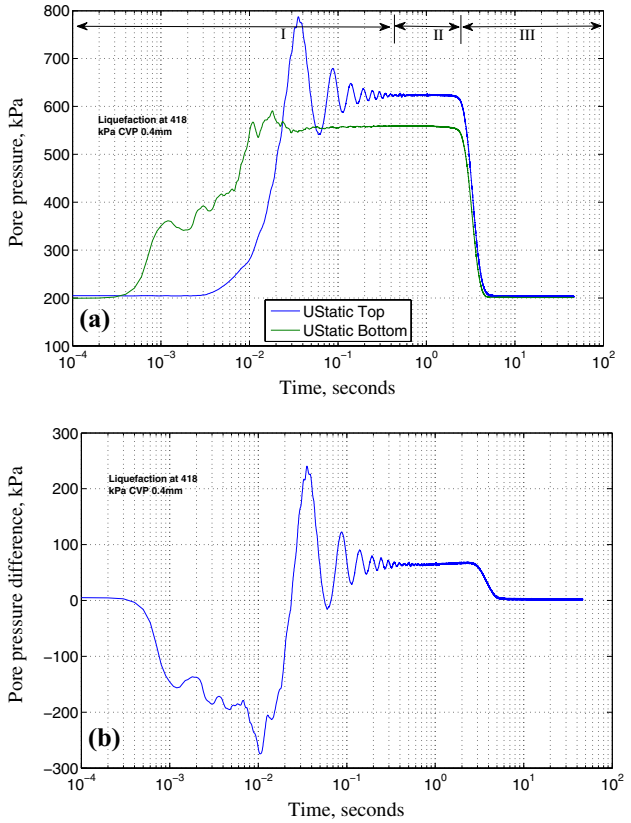

Fig. 10 **a** Temporal evolution of top and bottom static pore pressures, **b** pore pressure difference between top and bottom of isotropic liquefaction at 418 kPa of confining pressure on 0.4 mm CVP beads

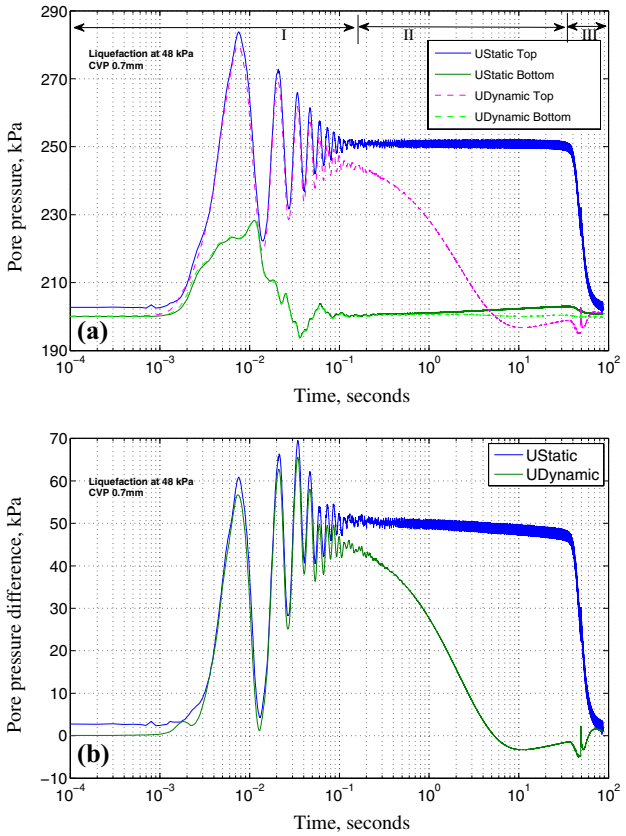

Fig. 11 **a** Temporal evolution of top and bottom dynamic and static pore pressures, **b** pore pressure difference between top and bottom of isotropic liquefaction at 48 kPa of confining pressure on 0.7 mm CVP beads

Figure 10a gives a very rare case of static top and bottom pore pressures of isotropic liquefaction occurring at 418 kPa on smaller 0.4 mm CVP beads. U_{top} confirms the three necessary conditions for instantaneous isotropic liquefaction on previous works [16]: a null effective stress during at least 1 s on a loose granular sample above a threshold void ratio e_{30}^{liq} at 30 kPa of confining pressure. U_{bottom} extends these same conditions for bottom pore pressure despite the full availability of the drainage system. The pore pressure difference in Fig. 10b stresses the non-homogenous effective stress state inside the sample for a liquefaction case. It also suggests the beginning of liquefaction within the upper part of the sample; then progressing downward to the lower end where the removal of the excess pore pressure is found.

This case paves the ways for the strong possibility of isotropic liquefaction in two-way drainage system on sample top and bottom, which has never been observed before in compression triaxial drained experiments.

Figure 11a shows another rare case of full static and dynamic pore pressure measurements of isotropic liquefaction at low pressure of only 48 kPa on standard 0.7 mm CVP beads, confirming once again the three necessary conditions and the validity of pore pressure measurements. Since the dynamic pore pressure sensor can not capture the stabilised plateau of U^{stable}, the dynamic top pore pressure (dashed line) quickly returns to the steady level of U^{stable} given by the static top pore pressure sensor. For small σ'_{trig} of 48 kPa, U_{bottom} quickly dissipates. However, the non-homogenous effective stress state and the constant phase *II* in Fig. 11 lasts exceptionally longer than 30s.

4.3 Undrained compression stick-slip

One similar question emerges following the existence of unconventional top pore pressure, especially the vibrating phase *I*: what happens for a closed system when no drainage is permitted, as in undrained triaxial test?

The effective stress path of an undrained triaxial compression at 100 kPa of confining pressure on 0.7 mm CVP beads is in Fig. 12a, showing for the first time the existence of large undrained compression stick-slip and globally the static liquefaction behaviour on very loose model granular materials. No collapse was noticed during this short isotropic consolidation step of only 100 kPa.

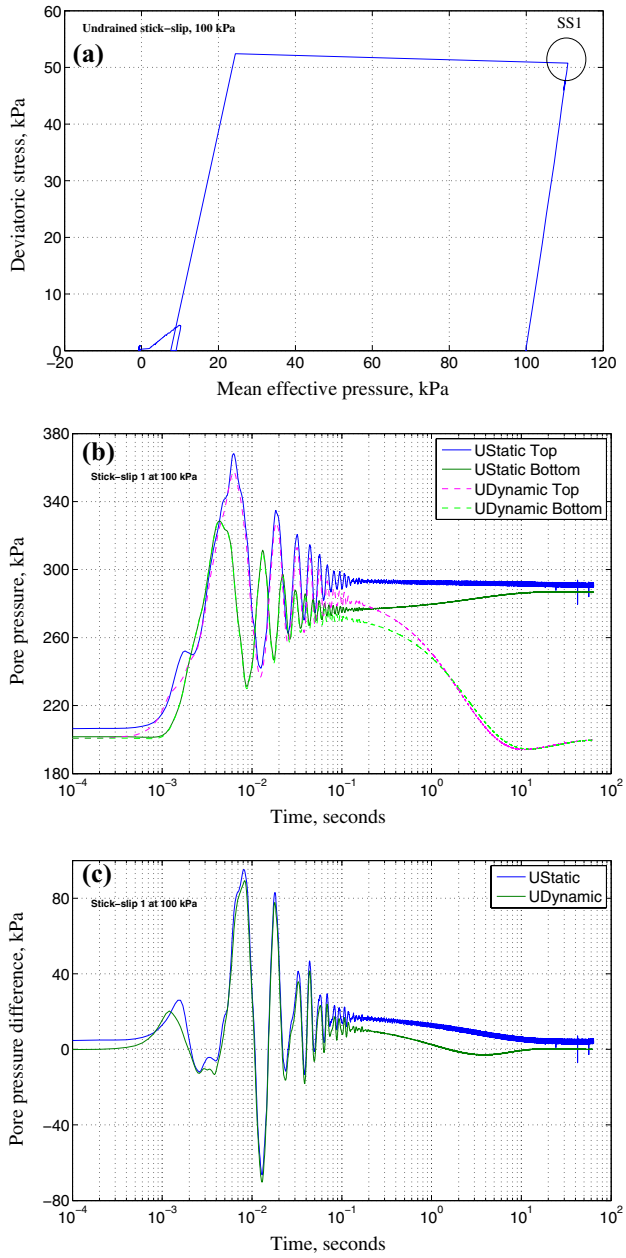

Fig. 12 **a** Effective stress path for undrained compression at 100 kPa of confining pressure, **b** temporal evolution of top and bottom dynamic and static pore pressures, **c** pore pressure difference between top and bottom of the first undrained stick-slip at 100 kPa on 0.7 mm CVP beads

Figure 12b exposes the unusual case of the first undrained compression stick-slip SS1 (large hollow circle) with a very fast and large reduction (92.4%) of effective confining pressure, reducing from 100 to only 7.6 kPa in one single step of a few seconds. As expected for a completely closed system, similar static top and bottom pore pressures are obtained with the indisputable presence of the first transient phase *I*, as detected simultaneously by the static and dynamic top and bottom pore pressure system. The stabilised U^{stable} after the vibrating phase remains unchanged, as anticipated for undrained test on a fully saturated granular assembly. Note the systematically smaller value of bottom pore pressure during the transient phase *I*, and slightly out of phase with respect to top pore pressure.

The pore pressure difference in Fig. 12c gets progressively smaller during the transient phase *I* and an homogenous effective stress state is practically attained after 10 s.

Consequently, the unattended pore fluid pressure outburst seems to be an unambiguously signature of the observed instabilities. The top static pore pressure can be used as a proxy in explaining the isotropic liquefaction and the axial strain jump of drained and undrained stick-slip behaviour in triaxial compression [1, 2, 10, 18, 76] or in direct shear [59] .

4.4 Characteristic time

The characteristic time t for this dynamic pore pressure dissipation can be estimated approximatively using the normalized excess pore pressure from the classical one-dimensional consolidation theory of Terzaghi [66], while disregarding the transient and stabilised phases *I* and *II*:

$$t = \frac{T_v H^2}{C_v};\ C_v = \frac{k(1+e_0)}{\gamma_w} * \frac{\Delta\sigma'}{\Delta e} \tag{1}$$

with C_v the consolidation coefficient, k the permeability, γ_w the fluid unit weight, $\Delta\sigma'$ the incremental effective stress, Δe the incremental void ratio from the initial value e_0 in isotropic compression testing, T_v the time factor and H the drainage height. The permeability of loose granular assembly can be independently determined by traditional falling head permeameter, $k = 2.6{*}10^{-4}$ m/s.

Upon ignoring the local collapses from Fig. 3, $C_v = 0.659$ m/s^2 and the characteristic time $t_{95} = 0.0084$ s for 95% of pore pressure dissipation can be estimated. Unfortunately, this roughly approximated time t_{95} is of about three orders of magnitude smaller than the average experimental characteristic time of 10 s in Fig. 7. In this over-simplification, t_{95} depends on the sample geometry, but not on grain diameter.

Taking into account the effect of grain diameter on k, the empirical formula of Carman-Kozeny [39] and the two-dimensional consolidation of a homogeneous granular cylinder can be achieved. Regrettably, the same order of magnitude difference remains. The notoriously difficult Biot's dynamic consolidation [5, 6] could be the next step to potentially overcome these difficulties.

4.5 Appearance conditions

What causes unusual isotropic collapses and drained compression stick-slips in model granular materials? In fact, the

existence of these instabilities on model geomaterials was not predicted, neither theoretically nor numerically, and their origins are still not well understood. The experiments in this paper show many additional unknown details of these still mysterious instabilities.

Concerning the appearance conditions for these dynamic instabilities, in addition to an initially structural anisotropic state revealed by high anisotropic coefficient during isotropic consolidation [16], we have already identified a threshold fabric void ratio at 30 kPa of confining pressure $e_{30}^{col} \approx e_{min}$, having a collapse-free behaviour during isotropic consolidation on dense dry or saturated samples (Fig. 17 in [15]). We have also identified a velocity-weakening behaviour [1, 14, 42] associated with a critical axial strain rate $\dot{\varepsilon}_a^{crit}$ (critical velocity in [4, 47]), about 2.5 mm/min for 50 kPa of cell pressure, indicating a total disappearance of stick-slip instability beyond $\dot{\varepsilon}_a^{crit}$ (Fig. 18 in [18]). Unfortunately, the estimated $\dot{\varepsilon}_a^{crit}$ exceeds the possibilities of our current equipment.

When replacing the usual incompressible de-aired pore water by highly compressible fluid like air, isotropic collapses and compression stick-slips are still observable on medium dense dry sample created by dry deposition method. The isotropic collapses extend the presence of stick-slip instability in literature [1, 11, 18] into the too often neglected case of isotropic compression, and confirm the paramount role of pore fluid viscosity [10, 60]. Two isotropic collapses are clearly detected at 62 and 197 kPa in Fig. 13a; and stick-slips with numerous precursors when sheared vertically at 500 kPa of confining pressure in Fig. 13b. The second collapse has a quite large incremental axial strain, of about 0.35%. Only axial strain was measured on this dry sample. Comparing to Fig. 4 on saturated samples, the striking feature still resides in the persistent presence of excess pore air pressure surge for all slip phases, however, very small value of about two orders of magnitude smaller with $\Delta U_{peak} \approx 0.5$ kPa was detected in Fig. 13c. Small oscillations are even recorded in transient phase with dynamic pore pressure sensor (not shown). Consequently, the lateral effective stress remains virtually unchanged and the deviatoric stress drop unaffected by ΔU. This small magnitude of excess pore pressure can partially explain the large number of small stick-slips, the small incremental axial strain developed during slip phase and the highly reduced liquefaction potential with no deviatoric stress drop to isotropic stress level for dry materials. However, a full analysis of isotropic collapse and stick-slip phenomenon including specific appearance conditions on dry model granular materials using high resolution data is out of scope for this paper.

One logical question emerges: Can these instabilities appear on used beads? It turns out, as typical preliminary results, that the third run on the same beads, although from a different batch, still gives very similar isotropic collapses

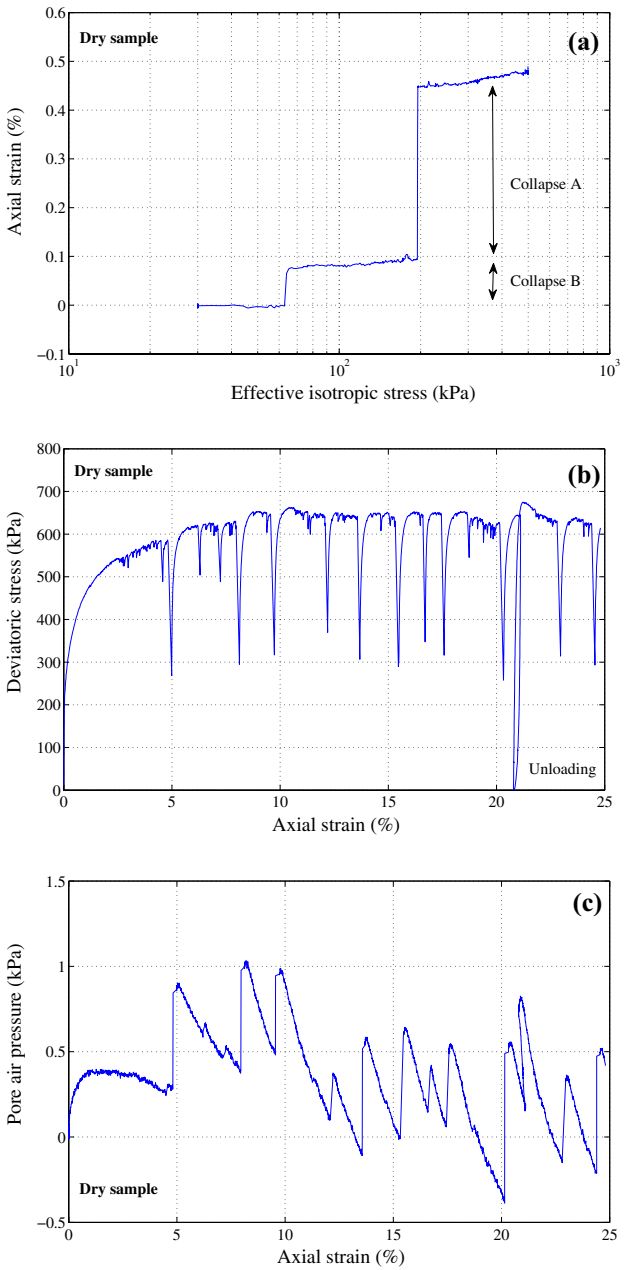

Fig. 13 **a** Isotropic consolidation with collapses at 62 and 197 kPa, **b** drained compression stick-slip behaviour with **c** pore air pressure at 500 kPa of confining pressure on dry medium dense specimen created by dry deposition method

and drained compression stick-slips in Fig. 14 at the same 500 kPa of confining pressure, comparing to virgin beads on Fig. 4. Nevertheless, many details differ, especially the triggering stress for collapses and the first stick-slip, due to the unpredictability of these instabilities in addition to some unknown wearing effects. Since no plausible explanation can be found to explain these discrepancies, this paper uses only virgin glass beads following the precautionary principle. It seems that the reproducibility of these dynamic events

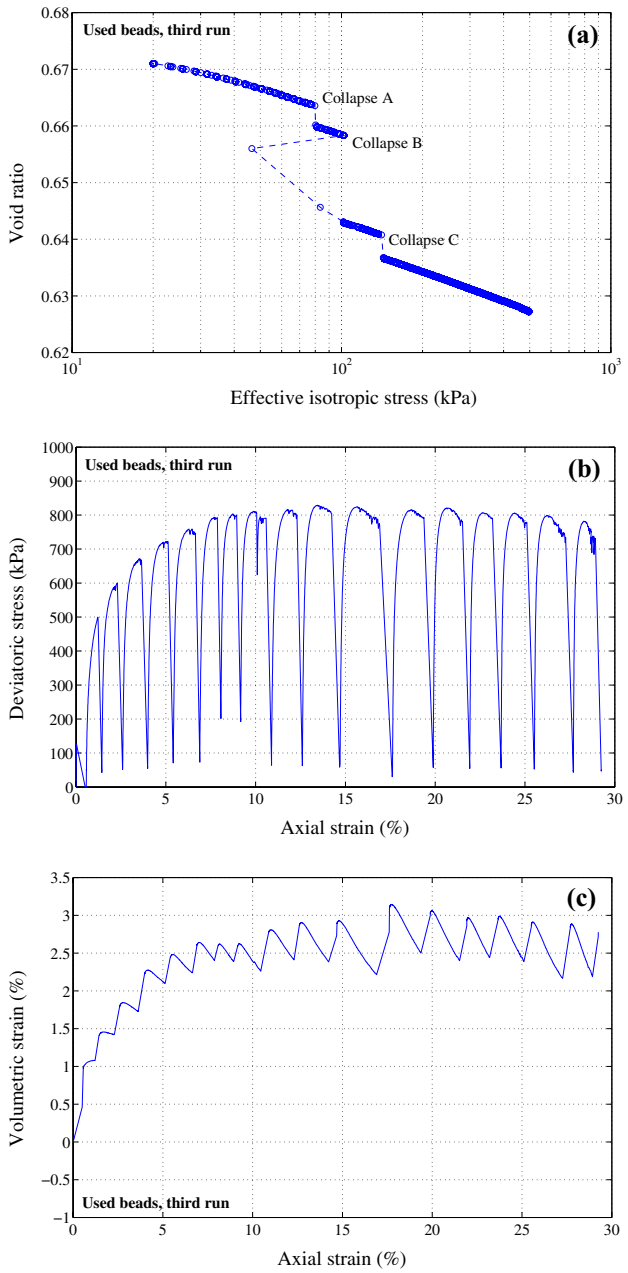

Fig. 14 **a** Isotropic consolidation with collapses at 80, 102 and 140 kPa, **b** drained compression stick-slip with **c** coupled volumetric behaviour at 500 kPa of confining pressure on the third run on saturated used glass beads

cannot be achieved with exactly identical results, even for virgin beads. Again, a full study of this subject is beyond the framework of the current investigation.

Smooth bead surface coated with Teflon can reduce drastically the mechanical properties of dense glass beads [74]; unfortunately, surface roughness was not precisely determined in this study. Additionally, subtle initial conditions might strongly influence brittle failure phenomena [32, 52]. We are planning to correlate the stick-slip behaviour with the bead's initial surface roughness measurements in future works.

Lastly, to our knowledge, these dynamic instabilities never happen for real granular materials (i.e. clean natural sands); and often soda-lime spherical glass beads were studied for having the same specific gravity as sands to facilitate the creation of very loose samples and to compare with numerical DEM simulations using standard spherical particles. PMMA, steel and rigid polystyrene beads are rarely used [21, 53, 56]. Furthermore, the effects of particle shape, in approximating the irregular profile of real granular particle, on the global mechanical behaviour still remain an open question [24, 75, 76]. Additionally, recent X-ray imaging on dry granular assembly under low confining stress of only 20 kPa shows a surprising large stress drop for elongated artificial particles and small one for spherical shape in stick-slip experiments using triaxial machine [46].

4.6 Plausible triggering mechanisms

The systematic delay between the pore pressure development ΔU and the deviatoric stress drop Δq in slip phase, of about 3 ms, in Fig. 8 excludes ΔU as the primary cause of slip instability. The briefness of slip phase, of about 2 ms in the same figure, suggests the structural instability of metastable microstructure within the granular assembly. This structural hypothesis seems to be plausible for both isotropic collapse and shear stick-slip due to the similarity of pore pressure generation, with the support of force chains carrying most of the applied stress using photo elastic materials [20, 41, 73].

Numerical simulations using DEM technique can offer some insights into the complexities of these instabilities from the formation, breakage and buckling of force chains, often considered as quasi-linear short chains of granular particles. Force chains are among the driving forces for the micro-structural evolution of granular medium [51, 67, 68, 78]. However, much of past DEM studies intentionally omit the presence of pore fluid that can surge under dynamic phenomena since the physics of these processes were poorly understood. Recently, numerical explorations show a crucial role of full solid–liquid coupling formulation [19, 25, 26] in the understandings of the observed phenomena.

Together, even without any direct observation, physical and numerical experiments give some quantitative support to the hydromechanical coupling mechanisms involving first the breakage of force chains supposed to generate a strong overpressure of pore fluid, then, this excess pore pressure reduces the effective stress in fully saturated media. Finally, the effective stress recovers during the pore pressure dissipation with a consequence of increasing axial and and volumetric strains.

While the force chain buckling is a promising scheme for a causative mechanism, alternate approach of local negative

second-work order is worth exploring within DEM simulations [49, 50]. These approaches can provide some useful links to the possible microscopic origins of the instabilities. Additionally, strong fluid flow in small migration channel between grains can have a role in destabilising the meta-stable granular structure [70]. Furthermore, recent experiments on similar catastrophic phenomena point out the possibility of some global structural rearrangements of the weak-contact granular networks in the bulk of 3D granular assemblies, acting as reliable quasi-periodic precursors to final avalanche of increasingly inclined granular slope [13, 32, 77]. Note that these avalanches have a quite well-defined triggering mechanism in the critical slope angle which is not our case.

Nevertheless, the key physical parameters that control this mechanical-induced pore pressure generation, either fluid or air, are still missing in these hypothetical scenarios, as well as the pore pressure evolution in the transient phase *I* and especially in the stable phase *II* leading to liquefaction case. Regardless of the adopted parameters, it will be a challenging task for DEM to consistently reproduce the observations during three distinct phases of the pore pressure evolution with different timescales and probably regulated by different physical processes.

5 Concluding remarks

The mechanical behaviour in drained isotropic and triaxial compression of loose, fully saturated monodisperse glass beads assembled by moist tamping and undercompaction method reveals the ubiquitous presence of dynamic instabilities, previously unknown in granular mechanics. These instabilities (i.e. isotropic collapse, compression stick-slip, and especially isotropic liquefaction) exhibit one common unexpected component in the sudden surge of excess pore pressure ΔU. This paper explores the key role of ΔU on the axial and volumetric strains of the dynamic collapse or slip component, following an in-depth verification of pore pressure measurement.

Three phases characterise each spontaneous instability occurring under uncontrolled isotropic or deviatoric triggering stress. A very fast ΔU is generated during the first short dynamic transient phase *I*, then oscillated like an underdamped system towards a stabilised top pore-water pressure ΔU^{stable}. The second phase *II* with a sustainable state of constant ΔU^{stable} can move the effective stress σ' downward to the null level of liquefaction if being maintained for some seconds. The sample deformation happens mostly in this phase, principally for the liquefaction case. The last dissipation phase *III* permits the recovery of σ' to the previous steady state before the instability event and resumes the instability cycle.

The unforeseen ΔU^{stable} is responsible for the development of the incremental axial and volumetric strains in an essentially dynamic consolidation process under constant deviatoric stress. Importantly, it can be linked to the evanescent first excess pore pressure peak ΔU^{peak}. The short-lived ΔU^{stable} is reliable, quadruple checked by top and bottom dynamic and static measurements at the end of the oscillating phase *I* and irrespective of loading condition. It shows a briefly non-homogenous effective stress state for less than one second. A plausible corresponding non-homogenous strain state remains a relevant open question.

However, this sudden surge of interstitial pore fluid is not the primary cause of the observed instabilities. In stick-slip experiment, ΔU^{stable} is in turn controlled by the normalised deviatoric stress drop in a linear relationship with high correlation coefficient. Nevertheless, how this excess pore pressure is generated, oscillated, propagated and maintained for a prolonged period of time—some seconds in the case of isotropic liquefaction—is still a mystery, as well as the main triggering mechanisms. While many details remain unknown, these up-to-date pore pressure observations in this paper can provide new clues.

This paper provides the first experimental evidence of the link between dynamic instabilities and short-lived pore pressure bursts. It validates the dynamic pore pressure measurements on the sample top and bottom and demonstrates the necessity of measuring the ephemeral ΔU^{stable}_{top} in order to partly understand and explain these observed dynamic instabilities.

The test data of this paper can be downloaded from the journal website as supplementary materials.

Acknowledgements Partial financial support of the first author provided by the Viet Nam Ministry of Education and Training through the VIED excellence scholarship program is fully acknowledged. We are indebted to V. Vidal and J.C. Géminard for estimating the characteristic time using Carman-Kozeny equation, to D. Mawer for his kind proofreading service and to anonymous reviewers for helpful comments.

Compliance with ethical standards

Conflict of interest There is no conflict of interest.

References

1. Adjemian, F., Evesque, P.: Experimental study of stick-slip behaviour. Int. J. Numer. Anal. Methods Geom. **28**(6), 501–530 (2004)
2. Alshibli, K.A., Roussel, L.E.: Experimental investigation of stick-slip behaviour in granular materials. Int. J. Numer. Anal. Methods Geom. **30**(14), 1391–1407 (2006)
3. Andreotti, B., Forterre, Y., Pouliquen, O.: Granular Media: Between Fluid and Solid. Cambridge University Press, Cambridge (2013)

4. Berman, A.D., Ducker, W.A., Israelachvili, J.N.: Experimental and theoretical investigations of stick-slip friction mechanisms. In: Tosati, E., Persson, B. (eds.) Physics of Sliding Friction, pp. 51–67. Kluwer Academic Publishers, Dordrecht (1996)
5. Biot, M.A.: Theory of propagation of elastic waves in a fluid-saturated porous solid. I. Low frequency range. J. Acoust. Soc. Am. **28**(2), 168–178 (1956)
6. Biot, M.A.: Theory of propagation of elastic waves in a fluid-saturated porous solid. II. Higher frequency range. J. Acoust. Soc. Am. **28**(2), 179–191 (1956)
7. Biswas, B., Ray, P., Chakrabarti, B.K.: Statistical Physics of Fracture, Breakdown and Earthquake. Wiley, London (2015)
8. Bjerrum, L., Krimgstad, S., Kummeneje, O.: The shear strength of a fine sand. In: Proceedings of 5th International Conference on Soil Mechanics and Foundation Engineering., vol. 1, pp. 29–37 (1961)
9. Bradley, B.A.: Strong ground motion characteristics observed in the 13 June 2011 M_w 6.0 Christchurch, New Zealand earthquake. Soil Dyn. Earthq. Eng. **91**, 23–38 (2016)
10. Çabalar, A.F., Clayton, C.R.I.: Some observations of the effects of pore fluids on the triaxial behaviour of a sand. Granul. Matter **12**(1), 87–95 (2010)
11. Cui, D., Wu, W., Xiang, W., Doanh, T., Chen, Q., Wang, S., Liu, Q., Wang, J.: Stick-slip behaviours of dry glass beads in triaxial compression. Granul. Matter **19**(1), 1 (2017)
12. Daouadji, A., Darve, F., Al Gali, H., Hicher, P.Y., Laouafa, F., Lignon, S., Nicot, F., Nova, R., Pinheiro, M., Prunier, F., Sibille, L., Wan, R.: Diffuse failure in geomaterials: experiments, theory and modelling. Int. J. Numer. Anal. Methods Geom. **35**(16), 1731–1773 (2011)
13. Delannay, R., Duranteau, M., Tournat, V.: Precursors and triggering mechanisms of granular avalanches. c. r. Phys. **16**(1), 45–50 (2015)
14. Dieterich, J.H.: Time-dependent friction and the mechanics of stick-slip. Pure Appl. Geophys. **116**(4), 790–806 (1978)
15. Doanh, T., Abdelmoula, N., Gribaa, L., Nguyên, T.T.T., Hans, S., Boutin, C., Le Bot, A.: Dynamic instabilities under isotropic compression of idealized granular materials. Acta Geotech. **12**(3), 657–676 (2017)
16. Doanh, T., Abdelmoula, N., Nguyên, T.T.T., Hans, S., Boutin, C., Le Bot, A.: Unexpected liquefaction under isotropic consolidation of idealized granular materials. Granul. Matter **18**(3), 67 (2016)
17. Doanh, T., Dubujet, Ph, Touron, T.: Exploring the undrained induced anisotropy of Hostun RF loose sand. Acta Geotech. **5**(4), 239–256 (2010)
18. Doanh, T., Hoang, M.T., Roux, J.-N., Dequeker, C.: Stick-slip behaviour of model granular materials in drained triaxial compression. Granul. Matter **15**(1), 1–23 (2013)
19. Dorostkar, O., Guyer, R.A., Johnson, P.A., Marone, C., Carmeliet, J.: On the role of fluids in stick-slip dynamics of saturated granular fault gouge using a coupled computational fluid dynamics-discrete element approach. J. Geophys. Res. Solid Earth **122**(5), 3689–3700 (2017)
20. Drescher, A., De Josselin de Jong, G.: Photoelastic verification of a mechanical model for the flow of a granular material. J. Mech. Phys. Solids **20**, 337–351 (1972)
21. Fall, A., Ovarlez, G., Hautemayou, D., Mzire, C., Roux, J.-N., Chevoir, F.: Dry granular flows : rheological measurements of the μ(I)-rheology. J. Rheol. **59**(4), 1065–1080 (2015)
22. Fragaszy, R., Voss, M.: Undrained compression behavior of sand. J. Geotech. Eng., ASCE **112**(3), 334347 (1986)
23. Gajo, A., Bigoni, D., Muir Wood, D.: Multiple shear band development and related instabilities in granular materials. J. Mech. Phys. Solids **52**(22), 2683–2724 (2004)
24. Garcia, X., Latham, J.-P., Xiang, J., Harrison, J.P.: A clustered overlapping sphere algorithm to represent real particles indiscrete element modelling. Géotechnique **59**(9), 779–784 (2009)
25. Goren, L., Aharonov, E., Sparks, D., Toussaint, R.: Pore pressure evolution in deforming granular material: a general formulation and the infinitely stiff approximation. J. Geophys. Res. **115**, B09216 (2010)
26. Goren, L., Aharonov, E., Sparks, D., Toussaint, R.: The mechanical coupling of fluid-filled granular material under shear. Pure Appl. Geophys. **168**(12), 2289–2323 (2011)
27. Gudehus, G., Jiang, Y., Liu, M.: Seismo- and thermodynamics of granular solids. Granul. Matter **13**(4), 319–340 (2011)
28. Hareb, H., Doanh, T.: Probing into the strain induced anisotropy of Hostun RF loose sand. Granul. Matter **14**(5), 589–605 (2012)
29. Heslot, F., Baumberger, T., Perrin, B., Caroli, B., Caroli, C.: Creep, stick-slip, and dry-friction dynamics: experiments and a heuristic model. Phys. Rev. E **49**(6), 4973–4988 (1994)
30. Igra, O., Seiler, F.: Experimental Methods of Shock Wave Research. Springer, New York (2016)
31. Iverson, R.M., LaHusen, R.G.: Dynamic pore-pressure fluctuations in rapidly shearing granular materials. Science **246**(4931), 796–799 (1989)
32. de Richter, S.K., Le Caër, G., Delannay, R.: Dynamics of rearrangements during inclination of granular packings: the avalanche precursor regime. J. Stat. Mech. **2012**, 4013 (2012)
33. Krehl, P.: History of Shock Waves, Explosions and Impact. Springer, New York (2009)
34. Kumar, N., Luding, S.: Memory of jamming—multiscale flow in soft and granular matter. Granul. Matter **18**(3), 58 (2016)
35. Ladd, R.S.: Preparing test specimens using undercompaction. Geotech. Test. J. **1**(1), 16–23 (1978)
36. Lade, P.V.: Triaxial Testing of Soils. Wiley, London (2016)
37. Lade, P.V., Duncan, J.M.: Cubical triaxial tests on cohesionless soil. J. Soil Mech. Found., ASCE **99**(10), 793–812 (1973)
38. Lagioia, R., Nova, R.: An experimental and theoretical study of the behaviour of a calcarenite in triaxial compression. Géotechnique **45**(4), 633–648 (1995)
39. Lambe, T.W., Whitman, R.V.: Soil Mechanics. Wiley, London (1969)
40. Le Bouil, A., Amon, A., McNamara, S., Crassous, J.: Emergence of cooperativity in plasticity of soft glassy materials. Phys. Rev. Lett. **112**, 246001 (2014)
41. Liu, C.H., Nagel, S.R., Schecter, D.A., Coppersmith, S.N., Majmudar, S.: Force fluctuations in bead packs. Science **269**(5223), 513–515 (1995)
42. Marone, C.: Laboratory-derived friction laws and their application to seismic faulting. Annu. Rev. Earth Planet. Sci. **26**, 643–696 (1998)
43. Mašín, D.: Asymptotic behaviour of granular materials. Granul. Matter **14**(6), 759–774 (2012)
44. Mcdowell, G.R., De Bono, J.P.: On the micro mechanics of one-dimensional normal compression. Géotechnique **63**(11), 895–908 (2013)
45. Michlmayr, G., Or, D.: Mechanisms for acoustic emissions generation during granular shearing. Granul. Matter **16**(5), 627–640 (2014)
46. Murphy, K.A., Dahmen, K.A., Jaeger, H.M.: Transforming mesoscale granular plasticity through particle shape. Phys. Rev. X **9**, 011014 (2019)
47. Nasuno, S., Kudrolli, A., Bak, A., Gollub, J.P.: Time-resolved studies of stick-slip friction in sheared granular layers. Phys. Rev. E **58**(2), 2161–2171 (1998)
48. Nasuno, S., Kudrolli, A., Gollub, J.P.: Friction in granular layers: hysteresis and precursors. Phys. Rev. Lett. **79**(5), 949–952 (1997)

49. Nicot, F., Daouadji, A., Laouafa, F., Darve, F.: Second-order work, kinetic energy and diffuse failure in granular materials. Granul. Matter **13**(1), 19–28 (2011)
50. Nicot, F., Daouadji, A., Laouafa, F., Darve, F.: Inertia effects as a possible missing link between micro and macro second-order work in granular media. Int. J. Solids Struct. **49**(10), 1252–1258 (2012)
51. Nicot, F., Xiong, H., Wautier, A., Lerbet, J., Darve, F.: Force chain collapse as grain column buckling in granular materials. Granul. Matter **19**(2), 18 (2017)
52. Oger, L., Vidales, A., Uñac, R., Ippolito, I.: Tilting process with humidity: DEM modeling and comparison with experiments. Granul. Matter **15**(5), 629–643 (2013)
53. Ovarlez, G.: Statique et rhéologie d'un milieu granulaire confiné. Thèse de doctorat, Université Paris XI, U.F.R. Scientifique d'Orsay (2002)
54. Popescu, R., Prevost, J.: Centrifuge validation of a numerical model for dynamic soil liquefaction. Soil Dyn. Earthq. Eng. **12**(2), 73–90 (1993)
55. Popescu, R., Prevost, J.: Comparison between VELACS numerical "Class A" predictions and centrifuge experimental soil test results. Soil Dyn. Earthq. Eng. **14**(2), 79–92 (1995)
56. Pozo, O., Fraysse, N., Olivi-Tran, N.: Ageing in the stick-slip motion for a humid granular medium. In: McNamara, S., Garcia-Rojo, R., Herrmann, H.J. (eds.) Powders and Grains, pp. 629–633. Rotterdam, A.A. Balkema (2005)
57. Radjaï, F., Roux, S.: Contact dynamics study of 2D granular media: critical states and relevant internal variables. In: Hinrichsen, H., Wolf, D.E. (eds.) The Physics of Granular Media, pp. 165–187. Wiley, Berlin (2004)
58. Schofield, A., Wroth, P.: Critical State Soil Mechanics. McGraw-Hill, New York (1968)
59. Scuderi, M.M., Carpenter, B.M., Johnson, P.A., Marone, C.: Poromechanics of stick-slip frictional sliding and strength recovery on tectonic faults. J. Geophys. Res. Solid Earth **120**(10), 6895–6912 (2015)
60. Scuderi, M.M., Carpenter, B.M., Marone, C.: Physicochemical processes of frictional healing: effects of water on stick-slip stress drop and friction of granular fault gouge. J. Geophys. Res. Solid Earth **119**(5), 4090–4105 (2014)
61. Seed, H.B., Martin, P.P., Lysmer, J.: Pore water pressure changes during soil liquefaction. J. Geotech. Eng., ASCE **102**(4), 323–346 (1976)
62. Sibille, L., Hadda, N., Nicot, F., Tordesillas, A., Darve, F.: Granular plasticity, a contribution from discrete mechanics. J. Mech. Phys. Solids **75**(6), 119–139 (2015)
63. Sitharam, T.G., Vinod, J.S.: Critical state behaviour of granular materials from isotropic and rebounded paths: DEM simulations. Granul. Matter **11**(1), 33–42 (2009)
64. Skempton, A.W., Taylor, R.N.: The pore pressure coefficients A and B. Géotechnique **4**(4), 143–147 (1954)
65. Teng, F.C., Ou, C.Y., Hsieh, P.G.: Measurements and numerical simulations of inherent stiffness anisotropy in soft Taipei clay. J. Geotech. Geoenviron. Eng. **140**(1), 237–250 (2014)
66. Terzaghi, K., Peck, R.P., Mesri, G.: Soil Mechanics in Engineering Practice, 3rd edn. Wiley, London (1996)
67. Tordesillas, A., Hilton, J.E., Tobin, S.T.: Stick-slip and force chain evolution in a granular bed in response to a grain intruder. Phys. Rev. E **89**, 042207 (2014)
68. Tordesillas, A., Zhang, J., Behringer, R.: Buckling force chains in dense granular assemblies: physical and numerical experiments. Geomech. Geoeng. Int. J. **4**(1), 3–16 (2009)
69. Ueng, T.-S., Lee, C.-A.: Pore pressure generation in saturated sand induced by one- and two-dimensional shakings. J. Geoeng. **10**(2), 53–61 (2015)
70. Varas, G., Vidal, V., Géminard, J.-C.: Venting dynamics of an immersed granular layer. Phys. Rev. E **83**(1), 011302 (2011)
71. Verruijt, A.: An Introduction to Soil Dynamics. Springer, New York (2010)
72. Welker, P., McNamara, S.: Precursors of failure and weakening in a biaxial test. Granul. Matter **13**(1), 93–105 (2011)
73. Wood, D.M., Lesniewska, D.: Stresses in granular materials. Granul. Matter **13**(4), 395–415 (2011)
74. Wu, K., Abriak, N., Becquart, F., Pizette, P., Rémond, S., Liu, S.: Shear mechanical behavior of model materials samples by experimental triaxial tests: case study of 4 mm diameter glass beads. Granul. Matter **19**(4), 65 (2017)
75. Yang, J., Luo, X.D.: Exploring the relationship between critical state and particle shape for granular materials. J. Mech. Phys. Solids **84**(22), 196–213 (2015)
76. Yang, J., Wei, L.M.: Collapse of loose sand with the addition of fines : the role of particle shape. Géotechnique **62**(12), 1111–1125 (2012)
77. Zaitsev, V., Richard, P., Delannay, R., Tournat, V., Gusev, V.E.: Pre-avalanche structural rearrangements in the bulk of granular medium: experimental evidence. Europhys. Lett. **83**(6), 64003 (2008)
78. Zhang, L., Nguyen, N.G.H., Lambert, S., Nicot, F., Prunier, F., Djeran-Maigre, I.: The role of force chains in granular materials: from statics to dynamics. Eur. J. Environ. Civ. Eng. **21**(7–8), 874–895 (2017)